EEET ECOLOGICAL ENGINEERING & ENVIRONMENTAL TECHNOLOGY

Ecological Engineering & Environmental Technology, 2026, 27(12), 163–176
https://doi.org/10.12912/27197050/240324
ISSN 2719–7050, License CC-BY 4.0

Received: 2026.09.05
Accepted: 2026.10.13
Published: 2026.11.02

Spatiotemporal environmental dynamics and predictive modeling of mining-driven land use/land cover change at the Muruntau Mine, Uzbekistan

Dilawez Ali[1*], Mohd Nazish Khan[2], Hana Syafi Raihan[3], Sinchan Banerjee[4], Ozodxon Mahmudovna Kuziboyeva[5], Bakhtiyor Meliev[6]

[1] Department of Geology, Samarkand State University, Samarkand, Uzbekistan
[2] Department of Physical Geography and Natural Resources, Samarkand State University, Samarkand, Uzbekistan
[3] Department of Geographic Information Science Faculty of Geography, Gadjah Mada University, Yogyakarta, Indonesia
[4] Department of Geography, School of Basic and Applied Sciences, Adamas University, Kolkata, West Bengal, India
[5] Department of Geography, Kokand State University, Kokand, Uzbekistan
[6] Department of Climate Change, Water Resources Management and Geomatics, Samarkand State University, Samarkand, Uzbekistan
[*] Corresponding author's e-mail: dilawezali007@gmail.com

ABSTRACT

Large-scale open-pit mining is a major driver of land-cover transformation in arid and semi-arid environments, yet few studies integrate spatial driver analysis with long-term predictive modeling in such landscapes. This study examines spatiotemporal land use/land cover (LULC) change at the Muruntau gold mine, Uzbekistan the world's largest open-pit gold mine operation using Landsat imagery from 1992, 2000, 2008, 2016, and 2024. LULC maps were classified with a Support Vector Machine classifier (overall accuracy 91.42%, Kappa = 0.884) across six classes: mine area, sparse vegetation, exposed rock, water, barren land, and built-up area. Five spatial drivers (distance to the open-pit mine, roads, and water bodies, plus elevation and slope) characterized the anthropogenic and topographic controls on LULC transitions and were integrated into a CA-Markov framework to simulate a business-as-usual scenario for 2032. Barren land declined by 20.0% between 1992 and 2024, accompanied by expansion of mine area (+35.5%), exposed rock (+42.0%), water bodies (+62.0%), and built-up area (+147.4%). Transition matrix analysis showed decreasing land-cover stability with decreasing barren-land persistence (0.94, 1992–2016; 0.88, 2016–2024) and increasing conversion to exposed rock. Spectral indices (SAVI, NSMI, NDTI, MBI, BSI) pointed out the southeastern sector as the main hotspot of surface disturbance. Barren land area is expected to decrease further to ~21,500 ha by 2032, while mine and exposed-rock areas continue to expand. These results offer a spatially explicit basis for land reclamation planning and environmental management in large-scale arid mining landscapes.

Keywords: Muruntau mine; LULC; remote sensing; CA-Markov model; environmental dynamics.

INTRODUCTION

One of the most important human-induced agents of change of the land surface is large-scale mining operations, especially in arid and semi-arid zones. The utilization of natural resources, though indispensable for economic development, often leads to drastic changes in the pattern of landscape and environmental systems. Mining at Muruntau started in 1967 by

the state-owned enterprise Navoi Mining and Metallurgical Combinat (NMMC, also known as NGMK in Russian), and the mining operation is the world's largest open-pit gold mine (Kempe et al., 2016). Research focus has been gradually shifting from large scale at territory or regional scale to environmentally fragile areas like wetland (Badamfirooz & Mousazadeh, 2019; Malik & Rai, 2019) river basin (Deng et al., 2015; Kabite et al., 2020) and other mining areas (Basommi et al., 2016; Kamga et al., 2020). Large-scale open-pit mining areas, especially those in arid and semi-arid regions, are particularly vulnerable because intensive mining activities may lead to dramatic changes in land cover patterns, vegetation conditions, soil surfaces, and hydrological processes, while the low natural resilience of these ecosystems may limit environmental recovery. The mining area landscape is characterized by mining and other human production activities. The large-scale development of mining areas can therefore result in substantial environmental changes, including land degradation, alteration of surface characteristics, disturbance of water resources, and increased ecosystem fragility. The land rehabilitation and reclamation of post-mining land subsidence have complicated effects on the structure, composition and function of ecosystem in mining area directly or indirectly. Analysis of driving forces can reveal the law of evolution and driving mechanism of regional LULC change (Bai et al., 2013; Kabite et al., 2020). Thus, understanding not only the magnitude and spatial pattern of LULC change but also the relative influence of its driving factors is important for the development of effective land reclamation strategies and sustainable land use management in long-term mining landscapes.

Geographic information systems (GIS) and remote sensing (RS) techniques provide useful methods to understand, analyze and monitor LULC over time in landscapes (Armin et al., 2020; Kotaridis & Lazaridou, 2018). These techniques have been widely applied to monitor and assess spatial and temporal changes in LULC (Hua, 2017; Mannan et al., 2019). In addition, Landsat periodic imagery data for a given area is a reliable data source that can be used for the estimation of LULC trends in the area. GIS and RS techniques can represent the spatial modeling methods (Nouri et al., 2014). Modeling, simulation and prediction of LULC changes using temporal–spatial data are therefore essential to improve LULC planning and management. However, forecasting future LULC dynamics in mining areas is difficult, as land-cover transitions are affected by multiple interacting environmental and anthropogenic factors, and can be highly heterogeneous across spatial scales. The analysis of driving factors of LULC change in environmentally fragile areas such as reservoir area (Guan et al., 2019; Jing'an et al., 2018) is often based on the logistic regression model mountainous area (Zhai et al., 2018), etc . And it is also mostly used for analysis of driving factors of urban land use change (Jiang et al., 2015; Mei et al., 2018). Using Conversion of Land Use and its Effects at Small regional extent (Markov) model we can take into account many kinds of factors, preset multiple scenarios and visualize spatial patterns of LULC under different scenarios (Sun et al., 2016; Waiyasusri et al., 2016).

The future trend of LULC (change) is scenario simulation based on prediction (Jing'an et al., 2018; Zhu et al., 2010). Thus, the scenario simulation is gradually evolving from a single model to multiple integrated models (Cheng et al., 2019; Zhou et al., 2020). Previous studies have shown that support vector machines (SVM) model has more ability to reveal the main driving forces and interaction mechanisms of LULC change (Petropoulos et al., 2013; Vlachogianni et al., 2025).

However, there are several methodological gaps in the assessment of mining landscapes, notwithstanding the increasing application of LULC simulation models. First, the spatial resolution for the driving-factor analysis is generally chosen based on data availability or subjective judgment rather than objectively evaluated. Second, the relationships between LULC transitions and their driving factors are usually analyzed independently from subsequent spatial simulation, which limits the integration of driving-force analysis with future scenario prediction. Third, few studies have systematically combined objective spatial-scale determination, machine-learning-based driving-factor analysis, and scenario-based Markov simulation for long-term land-use planning in large-scale arid areas (Alikhanov et al., 2024; Selmy et al., 2023). Addressing these gaps is particularly critical for the Muruntau mining region where decades of intensive gold mining have produced substantial and persistent landscape transformation.

This research is focus on the Muruntau mining area, a large-scale open-pit gold mining landscape in the arid region of Uzbekistan. First, the multi-temporal 30-m LULC data derived from Landsat were used to determine a suitable spatial resolution for driving-factor based analysis. Then, an SVM based approach was used to characterize the relationships between LULC changes and their potential driving factors at the selected spatial resolution. The results showed that the selected driving factors were very powerful in explaining the LULC changes. The information obtained was then integrated in a Markov-based modeling framework to simulate future LULC patterns. The modeling framework was calibrated against the observed 2024 LULC map and used to simulate future 2032 LULC patterns under different development scenarios. The results gave a scientific basis for land-reclamation planning, sustainable land-use management, and the optimum allocation and protection of land resources in the Muruntau mining area.

MATERIALS AND METHODS

Study area

The Muruntau mine contains gold deposit, which is located at 41°29′ N latitude and 64°34′ E longitude within the Kyzylkum desert in central-western Uzbekistan and the largest gold resource in Eurasia (Drew et al., 1996). As shown in (Fig. 1) it is some more than 400 km to the west of the capital, Tashkent, and is served by the adjacent town of Zarafshan. The natural vegetation of around the study area is sparse and dominated by drought and salt-tolerant shrubs, grasses and herbaceous species. Navoi's northern part is occupied by a vast desert. The desert is home to xerophytic and halophytic flora, while the vegetation around the Kyzlkum desert is sparse (Fig. 3).

A precise methodological framework is employed to analyze satellite imagery spanning multiple temporal periods. Key considerations encompassed the selection of cloud-free images, the assurance of high spatial resolution, and the maintenance of consistent acquisition dates. Subsequently, the images are projected using the Universal Transverse Mercator projection (UTM). Their geographic location is accurately determined using the World Geodetic System 1984 (WGS84) and the ellipsoid (Okiemute et al., 2018). Landsat 5 TM and Landsat 8 OLI satellite imagery were acquired for the years 1992, 2000, 2008, 2016, and 2024 from the USGS Earth Explorer (http://earthexplorer.usgs.gov/). Images with less than 10% cloud cover were selected to ensure data quality. All images were projected to UTM Zone 41N (WGS84) to ensure spatial consistency across scenes. A 30 m spatial resolution was adopted, consistent with the native resolution of the Landsat sensors used and with prior mining-LULC studies employing similar imagery.

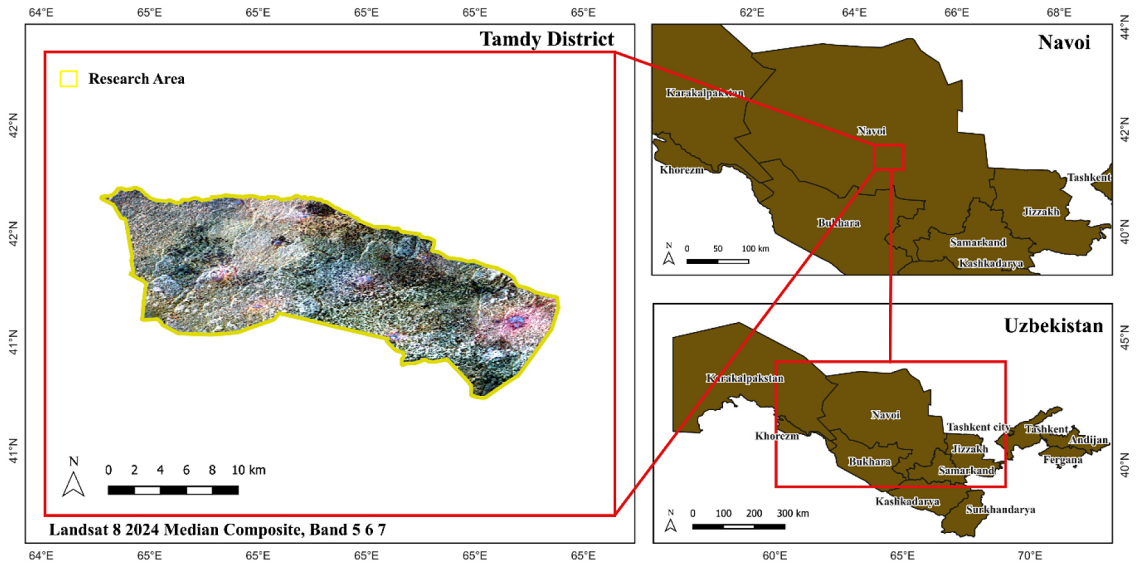

Figure 1. Maps showing mining in the research area. Maps were generated using ArcGIS 10.8 for desktop (http://www.esri.com/software/arcgis/arcgis-for-desktop)

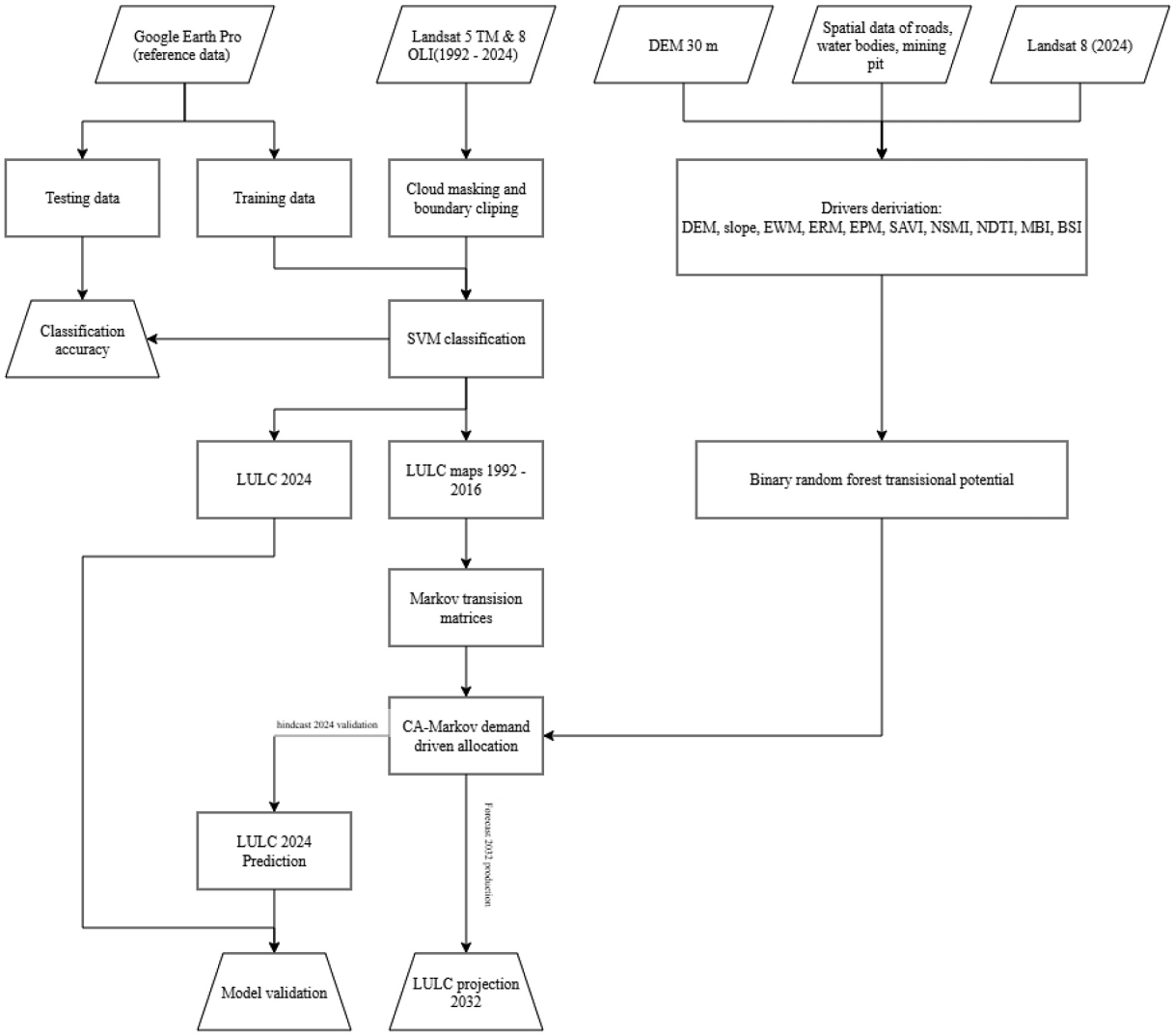

Figure 2. Diagram of the methodological process

Image processing

Preprocessing was performed using ArcGIS Desktop 10.8 (Nath et al., 2022). The workflow as shown in (Figure 2) included radiometric and geometric correction, cloud and shadow masking mosaicking, and clipping to the study area boundary. To maintain spectral consistency across sensors, Bands 2-5 (TM) and Bands 4-7 (OLI) were used.

Ground control points (GCPs) were identified using high-resolution imagery available in Google Earth Pro to support accurate geometric registration and spatial alignment of the 30 m Landsat datasets. For each study year, representative and homogeneous training polygons were manually delineated for each predefined LULC class. Training areas were selected to minimize mixed pixels and to capture the within-class spectral variability of the respective land-cover categories. Random sampling was subsequently applied to the training polygons, resulting in 181–533 training samples per year across the study periods.

The Landsat images were classified using a Support Vector Machine (SVM) classifier. SVM was selected because of its ability to effectively distinguish spectrally complex and nonlinearly separable land-cover classes, while maintaining good classification performance with relatively limited and heterogeneous training data. The classifier was trained using representative samples from each LULC class, and the resulting classification maps were visually inspected against high-resolution Google Earth Pro imagery to verify the spatial plausibility and consistency of the mapped land-cover patterns. Importantly, the visual comparison was used as an additional quality-control procedure, whereas quantitative accuracy assessment was conducted using independent validation samples that were not involved in model training.

Following classification, the LULC maps were subjected to accuracy assessment using independent reference samples. The validated raster datasets were subsequently converted to ASCII format using the *Raster to ASCII* tool in ArcGIS Desktop 10.8 to meet the input requirements of the subsequent spatial modeling procedures. The resulting LULC datasets were used to quantify historical land-cover transitions and to construct the transition probability matrices required for the CA-Markov model. The validated historical LULC maps were then used as inputs to simulate future spatial patterns of LULC under the specified development scenario.

Assessment of the accuracy

Evaluating the accuracy and reliability of image classification techniques is a crucial step in the research process (Lu & Lu, 2023). The studies have focused on the validation of the model and accuracy of making a reliable LULC survey (Ruuska et al., 2018). In this study Kappa statistics and total accuracy were used to evaluate the performance of classification maps. The land use map, land cover classification and ground reference data were used to calculate an error matrix. Some of the metrics identified are product accuracy, user accuracy, overall accuracy and Kappa coefficient (Foody, 2020). The overall accuracy was computed as the percentage of pixels that were correctly classified in the confusion matrix as Eq. (1). The Kappa index indicated the degree of agreement between the classified map and the reference data used (Twele et al., 2016). The two measures are calculated using the following equations:

$$Overall\ accuracy\ = \frac{D}{T} * 100\% \qquad (1)$$

where: D is the total number of correct calls summed along the major diagonal and T is the total number of correct calls in the error matrix.

The Kappa index is calculated as follows:

$$\{\kappa\} = \text{frac}\left\{ T \sum_{\{n=1\}}^{\{r\}Y}{}_{\{nn\}} - \sum_{\{n=1\}}^{\{r\}\left(Y_{\{n+\}Y_{\{+n\}}}\right)} \right\} \left\{ T^2 - \sum_{\{n=1\}}^{\{r\}\left(Y_{\{n+\}Y_{\{+n\}}}\right)} \right\} \qquad (2)$$

where: T is the total number of cells in the error matrix, r is the number of rows in the matrix, Y_{nn} is the total number of correct cells in a class (i.e., value in row n and column n), Y_{n+} is the total for row n, Y_{+n} is the total for column n.

Kappa indices are important tool to assess the accuracy of maps since they give information about how close the results are. Kappa values of 75% or above indicate high consistency between the maps, kappa values between 50%

Figure 3. Muruntau mine area, showing: (a) mine area, (b) sparse vegetation, and (c) barren land

and 75% indicate an average degree of agreement, and kappa values below or equal to 50% indicate poor agreement (El Baroudy, 2016; Rendana et al., 2015). Wang & Zheng (2023) simulated the land use and land cover in 2024 using the classified images from 1992 and 2024 to examine the ability of the CA-Markov model to predict the future land use and land cover states and validated the CA-Markov model. The validation module is used to compare the simulated area and real area of each land use and land cover class. The Kappa index is a suitable indicator; therefore, land use and land cover can be predicted for 2032.

Land use and land cover change detection

Analyzing these changes (LULCC) is essential to identify the particular changes in different land use categories (Spruce et al., 2020). The land cover change detection map is used to assess and examine the temporal changes in land use and land cover within the defined area. The equation Eq. (3) mentioned below is applied to estimate the size of the changes that occurred in each category:

$$C_i = R_i - B_i \tag{3}$$

where: Ci represents the change in extent for the class i, Bi denotes the base image, and Ri is the most recent image.

The percentage change for each LULC class is calculated using the following equation Eq. (4):

$$P_i = \frac{R_i - B_i}{B_i} \tag{4}$$

where: Pi denotes the percentage shift for the class i, and Bi denotes the base image, and R_i is the most recent image.

The classified LULC maps for 1992, 2000, 2008, 2016, 2024, and the projected 2032 scenario are presented in (Fig. 4), illustrating the spatial redistribution of land-cover classes across the study period. The corresponding areal extent and classification accuracy for each class and year are summarized in Table 1.

Spatial driver analysis to mining

The accuracy prediction of the CA-Markov model is highly dependent on the selection of appropriate spatial driving factors representing the dominant processes of LULC change. For the Muruntau mining area, five spatial drivers were selected: Euclidean distance to the open-pit mine,

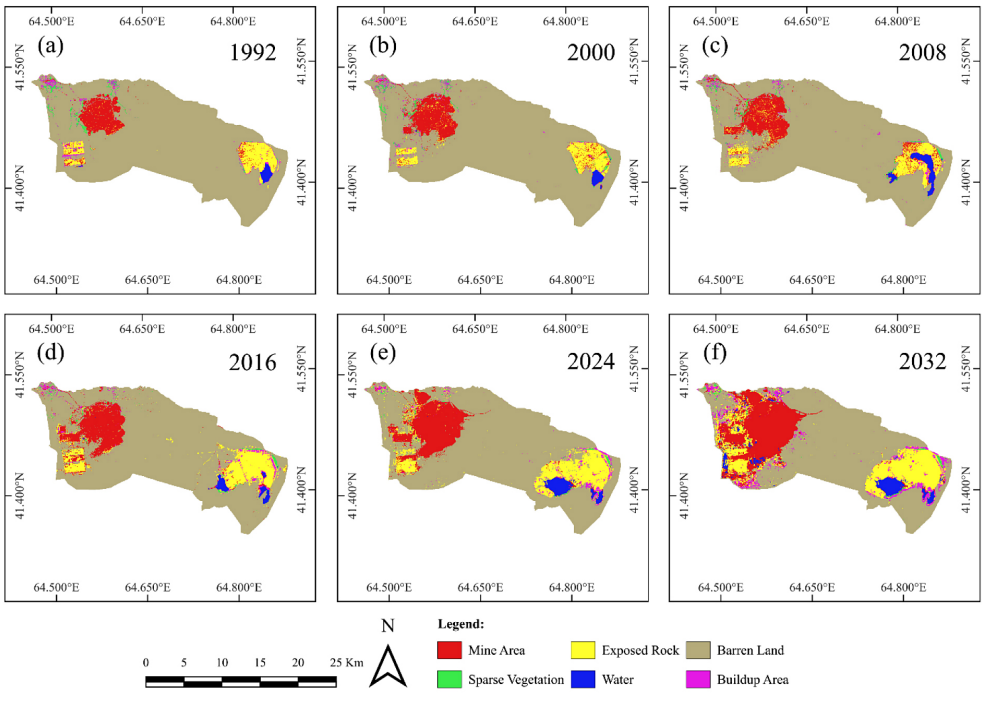

Figure 4. The LULC types maps of 1992, 2000, 2008 and 2016, 2024 and 2032. Maps were generated using ArcGIS 10.8 for desktop (http://www.esri.com/software/arcgis/arcgis-for-desktop)

Table 1. LULC classification for 1992, 2000, 2008, and 2016, 2024 and 2032

Year	Mine area	Sparse vegetation	Exposed rock	Water	Barren land	Built-up area	Overall accuracy, %	Kappa
1992	2472.66	404.91	2166.30	267.39	32468.40	568.53	92.27	0.9023
2000	3071.34	428.85	2140.56	251.55	31941.72	514.17	88.70	0.8460
2008	3655.26	392.67	2436.12	640.26	30685.41	538.47	89.43	0.8551
2016	4074.66	279.18	3740.31	435.51	29175.84	642.69	93.25	0.9082
2024	5279.04	214.65	4490.91	813.33	26848.35	701.91	93.48	0.9084
2032	7154.46	275.76	6378.75	1317.6	21485.43	1736.19	92.27	0.9023

Euclidean distance to roads, Euclidean distance to water bodies, elevation and slope. These variables are the main anthropogenic, accessibility, topographic and environmental controls of LULC transitions in arid mining landscape. Each variable was used as conditioning factor to assess the appropriateness of locations for transition between LULC classes based on the principle that the effect of anthropogenic features generally decreased with increasing distance.

Euclidean distance to the open-pit mine is a proxy of mining-related disturbance intensity and is expected to influence the expansion of disturbed land and waste-dumping areas. Euclidean Distance to roads is an indicator of accessibility and transportation networks that facilitate mining activities and built-up expansion. Topographic constraints include elevation and slope, which affect land-use suitability, construction feasibility, drainage, and erosion. In the water-limited Kyzyl

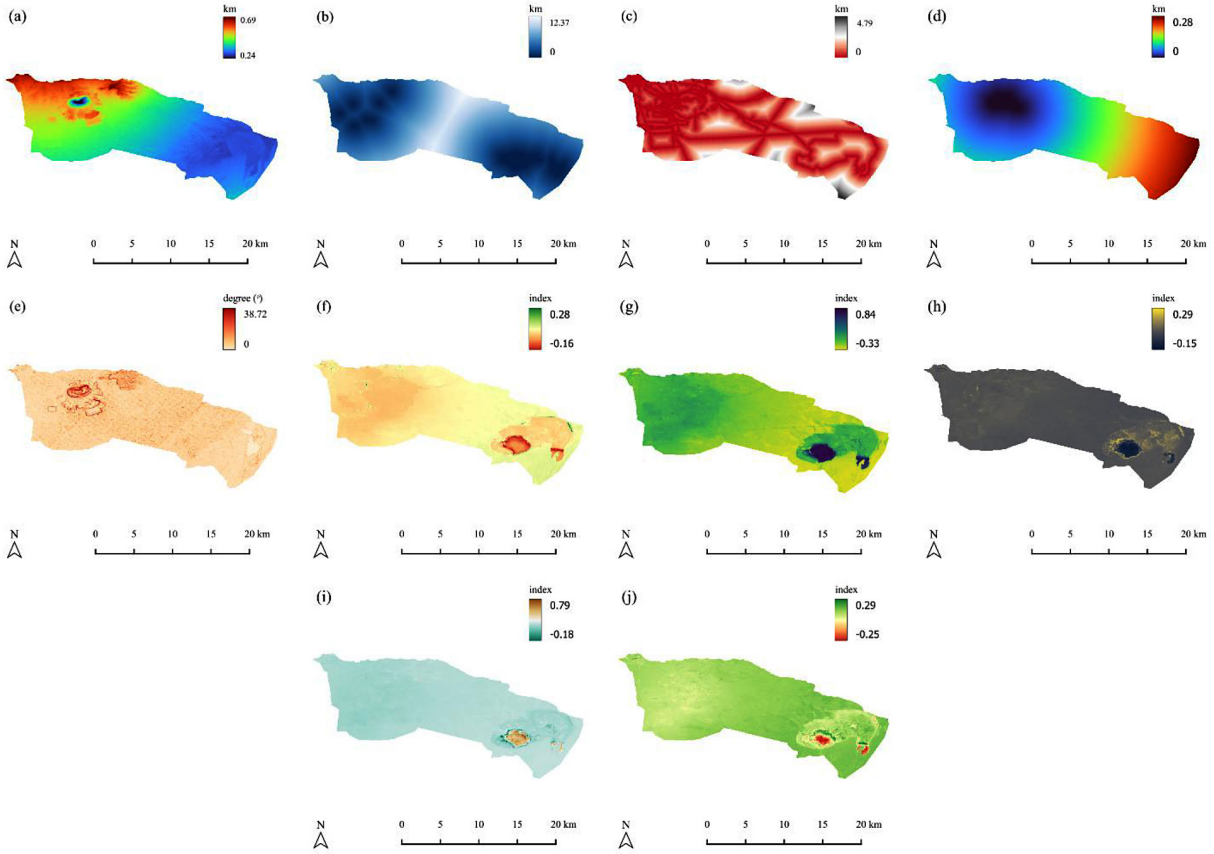

Figure 5. Spatial datasets used for the 30 m resolution GIS-based analysis prepared in ArcGIS: (a) digital elevation model (DEM), (b) Euclidean distance from water bodies (EWM), (c) Euclidean distance from roads (ERM), (d) Euclidean distance from mining pits (EPM), (e) slope, (f) soil adjusted vegetation index (SAVI), (g) normalized soil moisture index (NSMI), (h) normalized difference tillage index (NDTI), (i) modified bare soil index (MBI), and (j) bare soil index (BSI). All layers were generated at a spatial resolution of 30 m using ArcGIS

Kum Desert, the distribution of vegetation, development of settlements and mining activities are dependent on water availability, and therefore distance to water bodies is a significant environmental factor. The combined effect of these five driving factors provides a spatial explicit representation of the major physical and anthropogenic controls on LULC transitions and allows for realistic simulation of future landscape patterns in the Muruntau mining area.

In addition to these five spatial drivers and five spectral indices (SAVI, NSMI, NDTI, MBI and BSI) were computed to characterize vegetation, soil moisture, and surface disturbance; these indices were used for descriptive interpretation of degradation patterns in result section and were not included as inputs to the CA-Markov transition model.

Soil-adjusted vegetation index (SAVI): Vegetation greenness is one of the most important channels of measuring the health of an ecosystem, especially in drylands where the vegetation cover is thin and vulnerable to interference. Soil-Adjusted Vegetation Index (SAVI) was chosen over NDVI because it removes the problem of soil brightness under low vegetation cover which is also a common occurrence in the Kyzylkum Desert. SAVI is formulated as Eq. (5):

$$SAVI = \frac{(NIR - Red)}{(NIR + Red + L)}(1 + L) \quad (5)$$

where: (L = 0.5) is the soil adjustment factor. Larger SAVI values signify the denser and healthier vegetation, indicating lower environmental stress (Huete, 1988).

Normalized soil moisture index (NSMI): is a spectral index used to characterize variations in soil moisture from satellite reflectance. (Haubrock et al., 2008) proposed NSMI based on the difference between reflectances at two wavelengths as shown in Eq. (6):

$$NSMI = \frac{R_j - R_i}{R_j + R_i} \quad (6)$$

where: Rj is the reflectance at the higher wavelength and Ri is the reflectance at the lower wavelength. For Landsat applications, a commonly used SWIR formulation is NSMI=(SWIR1−SWIR2)/(SWIR1+SWIR2).

Normalized difference tillage index (NDTI): is used to characterize crop residue and tillage conditions because SWIR reflectance is sensitive to dry plant residues and soil characteristics. The index is calculated as Eq. (7):

$$NDTI = \frac{SWIR1 - SWIR2}{SWIR1 + SWIR2} \quad (7)$$

For Landsat, this corresponds approximately to reflectances near 1650 nm and 2215 nm. The index is attributed to (van Deventer et al., 1997), and was subsequently used extensively for tillage/residue mapping.

Modified bare soil index (MBI): was developed by (Nguyen et al., 2021) to enhance the detection of bare-soil surfaces and distinguish them from vegetation and built-up areas. It incorporates SWIR1, SWIR2 and NIR reflectance as in Eq. (8):

$$MBI = \frac{(SWIR_1 - SWIR_2 - NIR)}{(SWIR_1 + SWIR_2 + NIR + 0.5)} \quad (8)$$

Bare soil index (BSI): The direct effect of land degradation is soil exposure, especially in the regions where mining causes deforestation and compaction. Bare Soil Index (BSI) is a spectral contrast method used to improve the spectral difference between mineral surfaces, which is a product of visible and shortwave infrared as shown in Eq. (9):

$$BSI = \frac{(Red + SWIR) - (NIR + Blue)}{(Red + SWIR) + (NIR + Blue)} \quad (9)$$

Large values of BSI signify a lot of bare ground, disturbed ground, or manmade surfaces that are the indicators of environmental degradation in arid areas (Metternicht & Zinck, 2003).

LULC change prediction using Cellular Automata Markov model

The cellular automata-Markov (CA-Markov) model is a methodology that combines cellular automata and Markov chains. This approach aims to predict future trends and characteristics of LULC change. The model of cellular automata considers the uncertainty associated with various factors, including the model components' relationships, the model design, and the quality of the data used as input (Palmate et al., 2022). On the other hand, the CA-Markov approach concentrates on the local interactions of cells, considering their

behavior in space and time. This method benefits from suitable computational capabilities for dynamic simulation and visualization.

In this study, the CA-Markov model was implemented in custom Python 3 workflow in Google Colab (NumPy, SciPy, rasterio, scikit-learn). Transition suitability (transition-potential) maps for each LULC class were derived from a per-class binary Random Forest classifier (300 trees), trained to distinguish pixels that transitioned into the target class from those that did not, using driver variables evaluated at the beginning of each transition period. The per-class transition potentials were then combined with a 3×3 neighborhood contiguity term (β = 0.35) and a persistence term, and allocated under a demand-driven scheme in which the Markov chain defines the target pixel count (demand) per class at t+1 and a greedy attractiveness ranking fills that demand until exhausted.

RESULTS AND DISCUSSION

The Figure 5 presents a comprehensive multi-panel visualization of ten spatial datasets, generated at a 30-meter resolution in ArcGIS, to characterize the topographic, proximity, and spectral properties of the study area. The first row displays physical and distance-based variables: the digital elevation model (a) reveals an elevation gradient ranging from 0.24 to 0.69 km, while the Euclidean distance maps delineate the spatial influence of water bodies (b, up to 12.37 km), road networks (c, up to 4.79 km, clearly outlining the infrastructure), and mining pits (d, up to 0.28 km, highlighting concentrated extraction zones in the southeast). The slope map (e) indicates terrain steepness up to 38.72 degrees. The subsequent rows display derived spectral indices: the soil adjusted vegetation index (f) and normalized soil moisture index (g) map vegetation cover and soil moisture (ranging up to 0.84), respectively, with the latter identifying distinct high-moisture zones. Finally, the normalized difference tillage index (h), modified bare soil index (i), and bare soil index (j) effectively isolate surface disturbances, with the bare soil indices clearly demarcating areas of exposed earth (shown in brown and red hotspots) that spatially correspond to the identified mining areas. Each map is oriented with a north arrow and includes a 20 km scale bar for spatial reference.

Figure 6 illustrates the temporal evolution of the LULC classes between 1992 and 2024, together with the projected (2032) scenario. Barren land remained the dominant class throughout the study period but exhibited a continuous decline, decreasing from approximately 32,500 ha in 1992 to about 26,800 ha in 2024, and is projected to contract further to roughly 21,500 ha by 2032. In contrast, mine area more than doubled over the observation period, expanding from about 2,400 ha in 1992 to nearly 5,200 ha in 2024, and is expected to reach approximately 7,200 ha by 2032. Exposed rock followed a similar upward trajectory, increasing from around 2,100 ha to about 4,500 ha during 1992–2024 and projecting to roughly 6,300 ha in 2032. Water bodies and built-up area showed modest but steady gains, whereas sparse vegetation, a minor component throughout (< 500 ha), declined slightly over time. The persistence of these trends

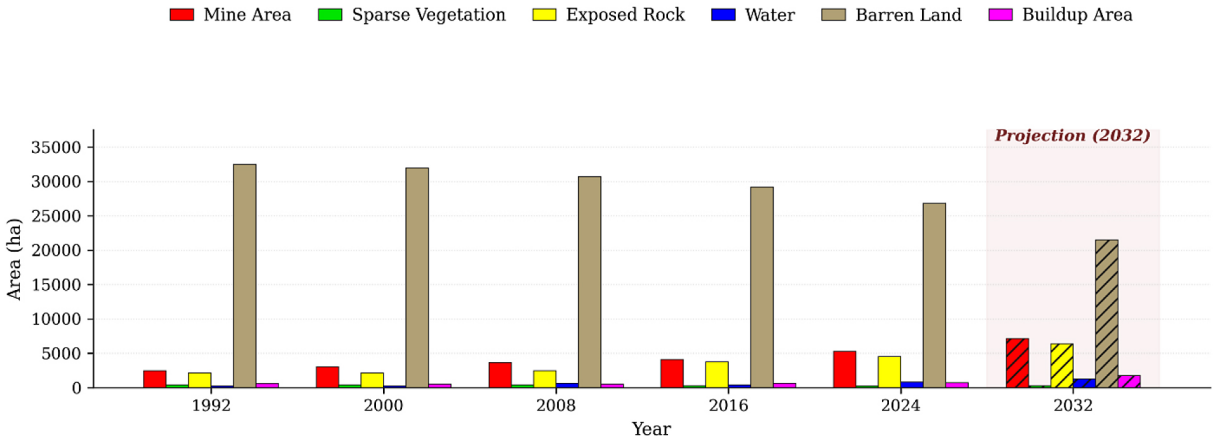

Figure 6. Temporal changes in land use/land cover (LULC) classes in the study area for 1992–2024, with the projected scenario for 2032

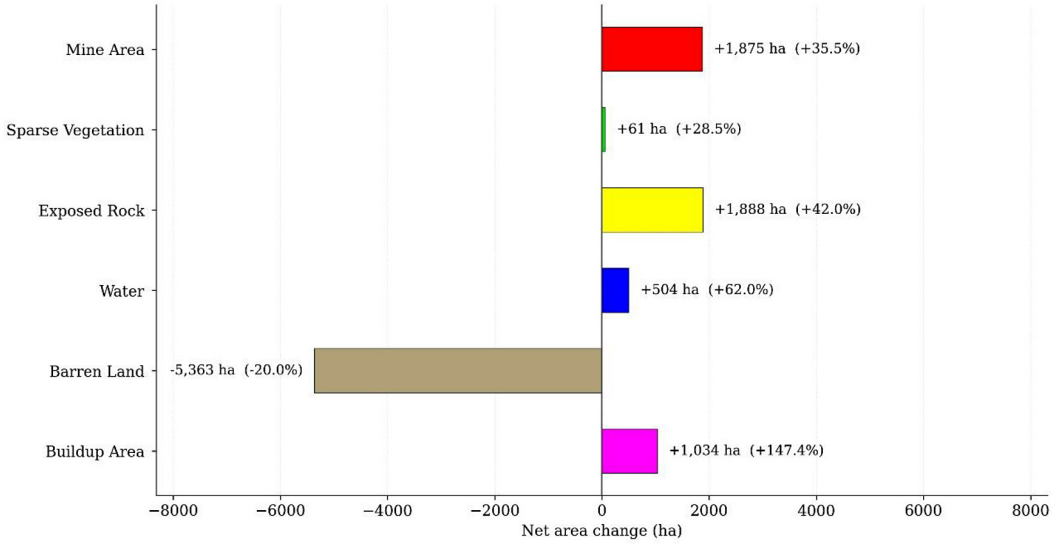

Figure 7. The LULC net change in area

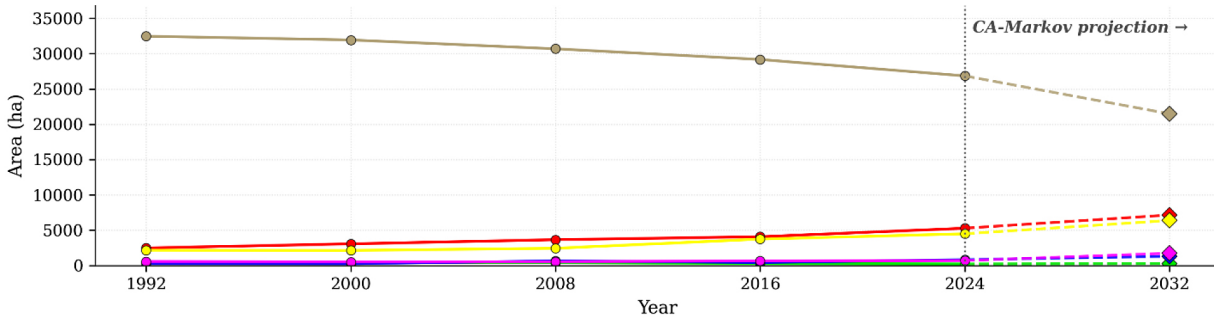

Figure 8. The change in area of LULC for the years 1992 to 2024 and 2032 is the predicted area by using the CA-Markov projection

in the 2032 projection indicates a progressive intensification of mining-related land disturbance.

The Figure 7 indicates that the analysis has shown a significant anthropogenic alteration of the landscape, mainly due to the large reduction in barren land (-5,363 ha; -20.0%), which has been extensively replaced by other land cover types. The biggest proportional increase was seen in urban areas (+1,034 ha, 147.4%), representing high rates of urban growth and infrastructure development. In parallel, large increases in both the size of the mines (+1,875 ha; +35.5%) and exposed rock (+1,888 ha; +42.0%) were found, reflecting high-intensity extractive operations and related surface disturbance. In addition, water bodies increased significantly by 62.0% (+504 ha) which may be due to hydrological changes caused by mining or water-filled excavations. All these changes together indicate an area in a state of fast change, caused by urban development and by mining, and with important consequences for land degradation and environmental management.

The transition matrices (Fig. 9) show the dynamics through time and stability of land cover classes over three different periods. The six land cover classes have different persistence and conversion probability. Barren land (0.94) and mine area (0.79) and exposed rock (0.65) were the less changeable land cover classes during the calibration period (1992–2016). But the transition patterns over the last five years (2016–2024) are different. The persistence of the mine area increased (0.86), and the stability of the barren land decreased slightly (0.88), indicating the increased rate of landscape changes. Water bodies were particularly volatile, moving substantially to exposed rock (0.47 in calibration; 0.16 in recent). Built-up areas had low persistence across all periods (0.41, 0.13 and 0.45 respectively), reflecting high rates of conversion to other land cover types, particularly exposed rock (0.45 in

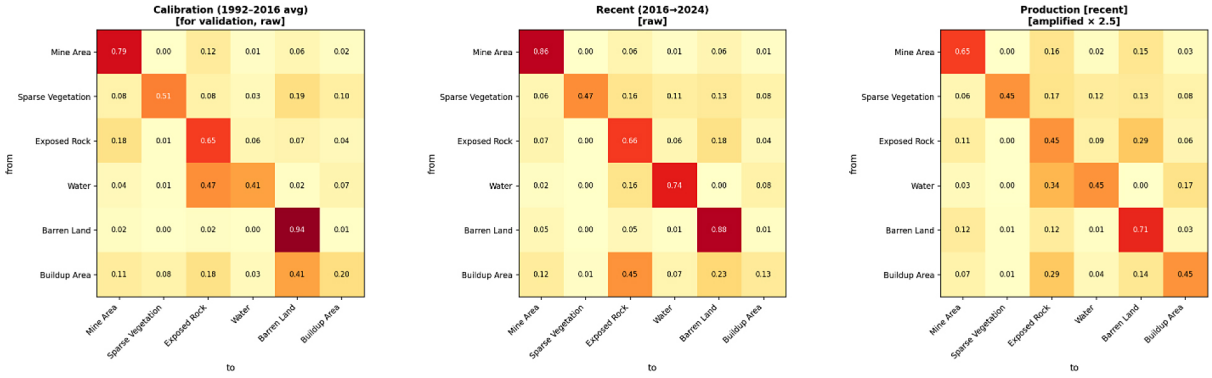

Figure 9. The transition matrices over LULC for three distinct period

recent). The production matrix with increased transition probabilities (x2.5) projects greater land cover dynamics with lower values of diagonal persistence (0.45–0.71) and higher off-diagonal transition probabilities, especially from barren land to exposed rock (0.29) and from water to exposed rock (0.34), together indicating a faster pathway of land degradation and surface modification in the following period. The overall classification accuracy was 91.42% and Kappa coefficient was 0.884 indicating substantial agreement between the classified and reference data set. Given this low classification reliability for the Built-up Area class, trends reported for this class (Fig. 6–8) should be interpreted with caution and are discussed as indicative rather than precise quantitative estimates.

Our predicted LULC changes are in line with the previous applications of the CA-Markov model in mining areas. CA-Markov has been found useful in predicting mining related land use/land cover (LULC) changes (Chang et al., 2021; Bensouda et al., 2026; Indawati et al., 2026). Similarly, studies in coal- and gold-mining regions have predicted future loss of vegetation, and expansion of disturbed land and environmental degradation with continued mining activities. The bare soil and low vegetation areas in the Huainan mining area are expected to increase in the future (Zhang et al., 2023). The results support the applicability of the CA-Markov for prediction of future LULC dynamics in mining-affected landscapes. However, the predictions are plausible scenarios under the influence of the intensity of mining, reclamation, policy, socioeconomic development, and climate variability.

Notably, the transition probabilities observed for 2016–2024 differ markedly from those of the 1992–2016 calibration period (Fig. 9), indicating that LULC transitions in this landscape are non-stationary. As the CA-Markov projection assumes stationary transition probabilities beyond the calibration period, the 2032 projection should be interpreted as one plausible trajectory rather than a precise forecast.

CONCLUSIONS

This study presents an integrated, spatially explicit assessment of LULC dynamics at the Muruntau mine for over three decades, integrating multi-temporal Landsat classification, driver-based spatial analysis, and CA-Markov simulation. The results showed significant anthropogenic change where barren land decreased by 20.0% from 1992 to 2024 and the mine area, exposed rock, water bodies, and built-up area increased with a proportional increase of 147.4% for built-up area. The Landsat imagery spectral indices (SAVI, NSMI, NDTI, MBI, BSI) consistently showed the southeast part of the study area to be the main surface disturbance area associated with active extraction and related infrastructure.

Transition-matrix analysis indicates that landscape stability has declined over time: barren land and mine area, the most persistent classes during the 1992–2016 calibration period, showed increased conversion rates in 2016–2024, while water bodies and built-up areas remained comparatively volatile throughout. Business-as-usual projections to 2032 suggest this trajectory will continue, with further contraction of barren land and expansion of mine area and exposed rock.

The results highlight the scale and speed of landscape change driven by mining in the Kyzyl Kum Desert, and indicate a definite need for

targeted land-reclamation planning, environmental monitoring and phased environmental restoration in the identified hotspot of degradation. Given the observed shift in transition probabilities between the calibration and recent periods, future work should treat Markov-based projections as one plausible trajectory rather than a fixed forecast, and should incorporate periodic recalibration as new imagery becomes available. The approach demonstrated here linking classified LULC data, spatial driver layers, and CA-Markov simulation offers a transferable framework for monitoring and planning in other large-scale arid mining landscapes facing similar pressures.

REFERENCES

1. Alikhanov, B., Pulatov, B., & Samiev, L. (2024). The Detection of Past and Future Land Use and Land Cover Change in Ugam Chatkal National Park, Uzbekistan, Using CA-Markov and Random Forest Machine Learning Algorithms. *Forum Geografi*, 38(2), 121–137. https://doi.org/10.23917/forgeo.v38i2.4221
2. Armin, M., Majidian, M., & Kheybari, V. G. (2020). Land Use/Land Cover Change Detection and Prediction in the Yasouj City Suburbs in Kohgiluyeh Va Boyerahmad Province in Iran. *Arid Ecosystems*, 10(3), 203–210. https://doi.org/10.1134/S2079096120030129
3. Badamfirooz, J., & Mousazadeh, R. (2019). Quantitative assessment of land use/land cover changes on the value of ecosystem services in the coastal landscape of Anzali International Wetland. *Environmental Monitoring and Assessment*, 191(11), 694. https://doi.org/10.1007/s10661-019-7802-8
4. Bai, J., Lu, Q., Wang, J., Zhao, Q., Ouyang, H., Deng, W., & Li, A. (2013). Landscape pattern evolution processes of alpine wetlands and their driving factors in the Zoige Plateau of China. *Journal of Mountain Science*, 10(1), 54–67. https://doi.org/10.1007/s11629-013-2572-1
5. Basommi, L. P., Guan, Q., Cheng, D., & Singh, S. K. (2016). Dynamics of land use change in a mining area: A case study of Nadowli District, Ghana. *Journal of Mountain Science*, 13(4), 633–642. https://doi.org/10.1007/s11629-015-3706-4
6. Bensouda Mourri, O., Baaba, M., Ouallal, A., Khazaza, A., Lakhili, F., El Amarty, F. & Benaabidate, L. (2026). Development of a 30 m spatiotemporal land use and land cover dataset (1985–2025) for the Allal El Fassi Watershed (Morocco) using Landsat time series and Google Earth Engine. *Ecological Engineering & Environmental Technology*, 27(10), 61–81. https://doi.org/10.12912/27197050/226297
7. Chang, X., Zhang, F., Cong, K., & Liu, X. (2021). Scenario simulation of land use and land cover change in mining area. *Scientific Reports*, 11(1), 12910. https://doi.org/10.1038/s41598-021-92299-5
8. Cheng, L., Sun, H., Zhang, Y., & Zhen, S. (2019). Spatial structure optimization of mountainous abandoned mine land reuse based on system dynamics model and CLUE-S model. *International Journal of Coal Science & Technology*, 6(1), 113–126. https://doi.org/10.1007/s40789-019-0241-x
9. Deng, Z., Zhang, X., Li, D., & Pan, G. (2015). Simulation of land use/land cover change and its effects on the hydrological characteristics of the upper reaches of the Hanjiang Basin. *Environmental Earth Sciences*, 73(3), 1119–1132. https://doi.org/10.1007/s12665-014-3465-5
10. Drew, L. J., Berger, B. R., & Kurbanov, N. K. (1996). Geology and structural evolution of the Muruntau gold deposit, Kyzylkum desert, Uzbekistan. *Ore Geology Reviews*, 11(4), 175–196. https://doi.org/10.1016/0169-1368(95)00033-X
11. El Baroudy, A. A. (2016). Mapping and evaluating land suitability using a GIS-based model. *CATENA*, 140, 96–104. https://doi.org/10.1016/j.catena.2015.12.010
12. Foody, G. M. (2020). Explaining the unsuitability of the kappa coefficient in the assessment and comparison of the accuracy of thematic maps obtained by image classification. *Remote Sensing of Environment*, 239, 111630. https://doi.org/10.1016/j.rse.2019.111630
13. Guan, D., Zhao, Z., & Tan, J. (2019). Dynamic simulation of land use change based on logistic-CA-Markov and WLC-CA-Markov models: A case study in three gorges reservoir area of Chongqing, China. *Environmental Science and Pollution Research*, 26(20), 20669–20688. https://doi.org/10.1007/s11356-019-05127-9
14. Haubrock, S. -N., Chabrillat, S., Lemmnitz, C., & Kaufmann, H. (2008). Surface soil moisture quantification models from reflectance data under field conditions. *International Journal of Remote Sensing*, 29(1), 3–29. https://doi.org/10.1080/01431160701294695
15. Hua, A. K. (2017). Land Use Land Cover Changes in Detection of Water Quality: A Study Based on Remote Sensing and Multivariate Statistics. *Journal of Environmental and Public Health*, 2017, 1–12. https://doi.org/10.1155/2017/7515130
16. Huete, A. R. (1988). A soil-adjusted vegetation index (SAVI). *Remote Sensing of Environment*, 25(3), 295–309. https://doi.org/10.1016/0034-4257(88)90106-X
17. Indawati, L., Setyono, P., Hikmayani, N. H. & Probandari, A. (2026). Spatiotemporal dynamics

of land cover before, during, and after the earthquake, using Sentinel-2 imagery and random forest classification. *Ecological Engineering & Environmental Technology*, 27(8), 217–232. https://doi.org/10.12912/27197050/225184

18. Jiang, W., Chen, Z., Lei, X., Jia, K., & Wu, Y. (2015). Simulating urban land use change by incorporating an autologistic regression model into a CLUE-S model. *Journal of Geographical Sciences*, 25(7), 836–850. https://doi.org/10.1007/s11442-015-1205-8
19. Jing'an, S., Yongfeng, D., Wei, W., & Shichao, Z. (2018). Simulation of future land-use scenarios in the Three Gorges Reservoir Region under the effects of multiple factors. *Journal of Geographical Sciences*, 28(12).
20. Kabite, G., Muleta, M. K., & Gessesse, B. (2020). Spatiotemporal land cover dynamics and drivers for Dhidhessa River Basin (DRB), Ethiopia. *Modeling Earth Systems and Environment*, 6(2), 1089–1103. https://doi.org/10.1007/s40808-020-00743-8
21. Kamga, M. A., Nguemhe Fils, S. C., Ayodele, M. O., Olatubara, C. O., Nzali, S., Adenikinju, A., & Khalifa, M. (2020). Evaluation of land use/land cover changes due to gold mining activities from 1987 to 2017 using landsat imagery, East Cameroon. *GeoJournal*, 85(4), 1097–1114. https://doi.org/10.1007/s10708-019-10002-8
22. Kempe, U., Graupner, T., Seltmann, R., De Boorder, H., Dolgopolova, A., & Zeylmans Van Emmichoven, M. (2016). The Muruntau gold deposit (Uzbekistan) – A unique ancient hydrothermal system in the southern Tien Shan. *Geoscience Frontiers*, 7(3), 495–528. https://doi.org/10.1016/j.gsf.2015.09.005
23. Kotaridis, I., & Lazaridou, M. (2018). Environmental Change Detection Study in the Wider Area of Lignite Mines. *Civil Engineering and Architecture*, 6(2), 108–114. https://doi.org/10.13189/cea.2018.060207
24. Lu, Z., & Lu, Y. (2023). Enhancing the reliability of image classification using the intrinsic features. *Knowledge-Based Systems*, 263, 110256. https://doi.org/10.1016/j.knosys.2023.110256
25. Malik, M., & Rai, S. C. (2019). Drivers of land use/cover change and its impact on Pong Dam wetland. *Environmental Monitoring and Assessment*, 191(4), 203. https://doi.org/10.1007/s10661-019-7347-x
26. Mannan, A., Liu, J., Zhongke, F., Khan, T. U., Saeed, S., Mukete, B., ChaoYong, S., Yongxiang, F., Ahmad, A., Amir, M., Ahmad, S., & Shah, S. (2019). Application of land-use/land cover changes in monitoring and projecting forest biomass carbon loss in Pakistan. *Global Ecology and Conservation*, 17, e00535. https://doi.org/10.1016/j.gecco.2019.e00535
27. Mei, Z., Wu, H., & Li, S. (2018). Simulating land-use changes by incorporating spatial autocorrelation and self-organization in CLUE-S modeling: A case study in Zengcheng District, Guangzhou, China. *Frontiers of Earth Science*, 12(2), 299–310. https://doi.org/10.1007/s11707-017-0639-y
28. Metternicht, G. I., & Zinck, J. A. (2003). Remote sensing of soil salinity: Potentials and constraints. *Remote Sensing of Environment*, 85(1), 1–20. https://doi.org/10.1016/S0034-4257(02)00188-8
29. Nath, B., Choudhury, N., & Mitra, A. K. (2022). Observing tectonic-geomorphological changes along the Dawki Fault and adjoining areas of Sylhet, Bangladesh from 1980 to 2020 using remote sensing and GIS techniques. *Journal of Earth System Science*, 131(3), 160. https://doi.org/10.1007/s12040-022-01900-6
30. Nguyen, C. T., Chidthaisong, A., Kieu Diem, P., & Huo, L.-Z. (2021). A Modified Bare Soil Index to Identify Bare Land Features during Agricultural Fallow-Period in Southeast Asia Using Landsat 8. *Land*, 10(3), 231. https://doi.org/10.3390/land10030231
31. Nouri, J., Gharagozlou, A., Arjmandi, R., Faryadi, S., & Adl, M. (2014). Predicting Urban Land Use Changes Using a CA–Markov Model. *Arabian Journal for Science and Engineering*, 39(7), 5565–5573. https://doi.org/10.1007/s13369-014-1119-2
32. Okiemute, E. S., Fatai, O. O., & Adekunle, O. S. (2018). Comparative Analysis of Three Geodetic Datum Transformation Software for Application between WGS84 and Minna Datums.
33. Palmate, S. S., Wagner, P. D., Fohrer, N., & Pandey, A. (2022). Assessment of Uncertainties in Modelling Land Use Change with an Integrated Cellular Automata–Markov Chain Model. *Environmental Modeling & Assessment*, 27(2), 275–293. https://doi.org/10.1007/s10666-021-09804-3
34. Petropoulos, G. P., Partsinevelos, P., & Mitraka, Z. (2013). Change detection of surface mining activity and reclamation based on a machine learning approach of multi-temporal Landsat TM imagery. *Geocarto International*, 28(4), 323–342. https://doi.org/10.1080/10106049.2012.706648
35. Rendana, M., Rahim, S. A., Idris, W. M. R., Lihan, T., & Rahman, Z. A. (2015). CA-Markov for Predicting Land Use Changes in Tropical Catchment Area: A Case Study in Cameron Highland, Malaysia. *Journal of Applied Sciences*, 15(4), 689–695. https://doi.org/10.3923/jas.2015.689.695
36. Ruuska, S., Hämäläinen, W., Kajava, S., Mughal, M., Matilainen, P., & Mononen, J. (2018). Evaluation of the confusion matrix method in the validation of an automated system for measuring feeding behaviour of cattle. *Behavioural Processes*, 148, 56–62. https://doi.org/10.1016/j.beproc.2018.01.004
37. Selmy, S. A. H., Kucher, D. E., Mozgeris, G., Moursy, A. R. A., Jimenez-Ballesta, R., Kucher, O.

D., Fadl, M. E., & Mustafa, A. A. (2023). Detecting, Analyzing, and Predicting Land Use/Land Cover (LULC) Changes in Arid Regions Using Landsat Images, CA-Markov Hybrid Model, and GIS Techniques. *Remote Sensing*, 15(23), 5522. https://doi.org/10.3390/rs15235522

38. Spruce, J., Bolten, J., Mohammed, I. N., Srinivasan, R., & Lakshmi, V. (2020). Mapping Land Use Land Cover Change in the Lower Mekong Basin From 1997 to 2010. *Frontiers in Environmental Science*, 8, 21. https://doi.org/10.3389/fenvs.2020.00021
39. Sun, P., Xu, Y., Yu, Z., Liu, Q., Xie, B., & Liu, J. (2016). Scenario simulation and landscape pattern dynamic changes of land use in the Poverty Belt around Beijing and Tianjin: A case study of Zhangjiakou city, Hebei Province. *Journal of Geographical Sciences*, 26(3), 272–296. https://doi.org/10.1007/s11442-016-1268-1
40. Twele, A., Cao, W., Plank, S., & Martinis, S. (2016). Sentinel-1-based flood mapping: A fully automated processing chain. *International Journal of Remote Sensing*, 37(13), 2990–3004. https://doi.org/10.1080/01431161.2016.1192304
41. Van Deventer, A. P., Ward, A. D., Gowda, P. H., & Lyon, J. G. (1997). Using Thematic Mapper Data to Identify Contrasting Soil Plains and Tillage Practices. *Photogrammetric Engineering & Remote Sensing* 63(1):87-93.
42. Vlachogianni, S., Servou, A., Karalidis, K., Paraskevis, N., Menegaki, M., & Roumpos, C. (2025). Remote sensing-based monitoring of land use and cover dynamics in surface lignite mining regions: A supervised classification approach. *Earth Science Informatics*, 18(2), 256. https://doi.org/10.1007/s12145-025-01781-5
43. Waiyasusri, K., Yumuang, S., & Chotpantarat, S. (2016). Monitoring and predicting land use changes in the Huai Thap Salao Watershed area, Uthaithani Province, Thailand, using the CLUE-s model. *Environmental Earth Sciences*, 75(6), 533. https://doi.org/10.1007/s12665-016-5322-1
44. Wang, S., & Zheng, X. (2023). Dominant transition probability: Combining CA-Markov model to simulate land use change. *Environment, Development and Sustainability*, 25(7), 6829–6847. https://doi.org/10.1007/s10668-022-02337-z
45. Zhai, H., Tang, X., Wang, G., Li, J., & Liu, K. (2018). Characteristic analyses, simulations and predictions of land use in poor mountainous cities: A case study in the central area of Chengde County, China. *Environmental Earth Science*s, 77(16), 585. https://doi.org/10.1007/s12665-018-7768-9
46. Zhang, X., Zhou, Y., Long, L., Hu, P., Huang, M., Chen, Y., & Chen, X. (2023). Prediction of the spatiotemporal evolution of vegetation cover in the Huainan mining area and quantitative analysis of driving factors. *Environmental Monitoring and Assessment*, 195(6), 776. https://doi.org/10.1007/s10661-023-11385-5
47. Zhou, L., Dang, X., Sun, Q., & Wang, S. (2020). Multi-scenario simulation of urban land change in Shanghai by random forest and CA-Markov model. *Sustainable Cities and Society*, 55, 102045. https://doi.org/10.1016/j.scs.2020.102045
48. Zhu, Z., Liu, L., Chen, Z., Zhang, J., & Verburg, P. H. (2010). Land-use change simulation and assessment of driving factors in the loess hilly region—A case study as Pengyang County. *Environmental Monitoring and Assessment*, 164(1–4), 133–142. https://doi.org/10.1007/s10661-009-0880-2